Journal of
Materials Chemistry A

ROYAL SOCIETY OF CHEMISTRY

Carrier density control in $Cu_2HgGeTe_4$ and discovery of Hg_2GeTe_4 *via* phase boundary mapping

SCHOLARONE™
Manuscripts

ROYAL SOCIETY OF CHEMISTRY

Journal Name

ARTICLE TYPE

Carrier density control in $Cu_2HgGeTe_4$ and discovery of Hg_2GeTe_4 *via* phase boundary mapping

Brenden R. Ortiz,[*a] Kiarash Gordiz,[a] Lídia C. Gomes,[b,c] Tara Braden,[a] Jesse Adamczyk,[a] Jiaxing Qu,[b,c] Elif Ertekin,[b,c] and Eric S. Toberer[*a]

The optimization and application of new functional materials depends critically on our ability to manipulate the charge carrier density. Despite predictions of good n-type thermoelectric performance in the quaternary telluride diamond-like semiconductors (e.g. $Cu_2HgGeTe_4$), our prior experimental survey indicates that the materials exhibit degenerate p-type carrier densities ($>10^{20}\,h^+cm^{-3}$) and resist extrinsic n-type doping. In this work, we apply the technique of phase boundary mapping to the $Cu_2HgGeTe_4$ system. We begin by creating the quaternary phase diagram through a mixture of literature meta-analysis and experimental synthesis, discovering a new material (Hg_2GeTe_4) in the process. We subsequently find that Hg_2GeTe_4 and $Cu_2HgGeTe_4$ share a full solid solution. An unusual affinity for Cu_{Hg} and Hg_{Cu} formation within $Cu_2HgGeTe_4$ leads to a relatively complex phase diagram, rich with off-stoichiometry. Through subsequent probing of the fourteen pertinent composition-invariant points formed by the single-phase region, we achieve carrier density manipulation ranging from degenerate ($>10^{21}\,h^+cm^{-3}$) to non-degenerate ($<10^{17}\,h^+cm^{-3}$) *via* manipulation of native defect formation. Furthermore, this work extends the concept of phase boundary mapping into the realm of solid solutions and clearly demonstrates the efficacy of the technique as a powerful experimental tool within complex systems.

1 Introduction

The optimization and application of new materials depends critically on our ability to manipulate the charge carrier density. Material development is often hindered, sometimes fatally, by our ability to dope. Consider, for example, the p-type doping of GaN. Natively n-type, p-type GaN was considered synthetically impossible for many years. The discovery of a unique combination of techniques, however, eventually enabled the widespread manufacturing of blue LEDs and secured a Nobel Prize.[1,2] In fact, the facile bipolar dopability of our most mature unary and binary diamond-like semiconductors (e.g. Si, GaAs) appears to be the exception and not the rule. Doping is a pervasive challenge that cuts across many fields. For example, the performance of thermoelectrics, photovoltaics, and superconductivity all hinge dramatically on doping. Advances in computational efforts and the application of concepts like machine-learning promise to accelerate our ability to dope new materials. Complementary experimental techniques will be required to validate and augment computational efforts.

Our prior high-throughput computational survey of the Inorganic Crystal Structure Database (ICSD) revealed a variety of potentially promising thermoelectric materials.[3] Among these materials were the series of quaternary diamond-like semiconductors (DLS) $Cu_2II_BIVTe_4$ (II_B: Zn, Cd, Hg)(IV: Si, Ge, Sn). Our prior work indicated that the quaternary DLS present as degenerately doped ($>10^{20}\,h^+cm^{-3}$) p-type semiconductors with unusually low thermal conductivity (<0.25 W/mK at 300°C) in Hg-containing compositions.[4] Together, our computational and experimental results confirmed that the Hg-containing DLS may be a potentially interesting class of p-type thermoelectric materials.[4] Interestingly enough, further analysis of our computational results suggests that the n-type behavior of these materials should *far surpass* the p-type behavior, owing to a large increase in the electronic mobility. A comparison of p-type and n-type results is included in the ESI (Table S1) for convenience, although all computational results are available on our open-source website TEDesignLab.org.[5] Unfortunately, reducing the carrier concentration to optimize the p-type transport was sufficiently difficult that n-type doping was considered altogether unlikely.

As one of the most technologically relevant classes of materials, the DLS have been the impetus for numerous computational studies aimed at broadly understanding, controlling, or calculating defects.[6-11] The photovoltaic community, in particular, has invested heavily in understanding doping and defect formation

[a] *Colorado School of Mines, Golden, CO, United States.*
[b] *University of Illinois at Urbana-Champaign, Urbana, Illinois, United States*
[c] *National Center for Supercomputing Applications, Urbana, Illinois, United States*
† Electronic Supplementary Information (ESI) available: [details of any supplementary information available should be included here]. See DOI: 10.1039/b000000x/

within ternary and quaternary DLS like $Cu(In,Ga)Se_2$ [12–20] and $Cu_2ZnSn(S,Se)_2$, [21–32] respectively. The problem has been sufficiently complex that significant challenges in optoelectronic performance persist to this day. Within thermoelectrics, the chemical diversity and complex defect formation in the DLS make them attractive candidate materials. The nuanced interplay between the effect of defects on the electronic mobility, thermal conductivity, and carrier density is an outstanding problem in the field. Many experimental studies on bulk ternary (e.g. $CuInTe_2$, [33–36] $AgGaTe_2$, [37] $CuFeS_2$, [38,39]) and quaternary (e.g. Cu_2CoSnS_4, [40] $Cu_2CdSnSe_4$, [41–44] $Cu_2ZnSnSe_4$ [45,46]) systems have utilized the rich defect chemistry (off-stoichiometry, vacancy doping, interstitials, extrinsic doping) in the DLS to optimize the thermoelectric performance.

This work tackles the challenge of doping in the quaternary diamond-like semiconductor $Cu_2HgGeTe_4$ through the process of phase boundary mapping. At its core, phase boundary mapping (PBM) leverages thermodynamics to probe the relationship between composition, phase competition, and the underlying defect structures. First coined to describe the process that enabled n-type doping of Mg_3Sb_2, [47] phase boundary mapping is starting to be applied in more complex systems like the Zintl ternary $Ca_9Zn_4Sb_9$, [48] and the mixed-anion skutterudite $Co_9Sn_4Te_4$. [49] A multitude of other studies (e.g. Zn_4Sb_3, [50] In-filled $CoSb_3$, [51] Bi_2Te_3, [52] Mg_2Si [53]) have also observed effects consistent with phase boundary mapping, although they were not described as such. To date, there has not been a phase boundary mapping study on a quaternary system. While carrier density manipulation is a key focus of this study, we also aim to advance the method of phase boundary mapping within quaternary systems and complex alloys.

Phase boundary mapping can be distinguished from more conventional studies by the intentional preparation of multi-phase samples. By leveraging the presence of impurities, we are able to fix the native chemical potentials within the sample. Not only does phase boundary mapping create a repeatable, well-defined way to probe the compositional extrema of a single-phase region, but it naturally synergizes with the language of defect calculations, where available. For simplicity, we begin by demonstrating the principle of phase boundary mapping on a toy ternary diagram (Figure 1a).

Consider synthesis of a sample (Figure 1a, black dot) within the three-phase region bound by ABC, B, and C. For simplicity, consider only trace impurities of B and C in an ABC matrix. The composition of ABC in this sample will be naturally fixed to the apex of the single-phase region defined by the phase equilibria. This point (Figure 1a, red dot) is defined as the composition-invariant point (shortened to c-invariant point), This approach is immune to small deviations in stoichiometry – as long as the overall composition falls within the three-phase region, ABC will *always* be fixed to the same composition. Synthesis within the single-phase or two-phase regions do not enjoy this effect, and will be dependent on precise stoichiometry control. Confirmation of the c-invariant point is straightforward, as the impurities can be easily detected by diffraction and microscopy. The process is repeated for every Alkemade triangle (4 total in Figure 1a). This
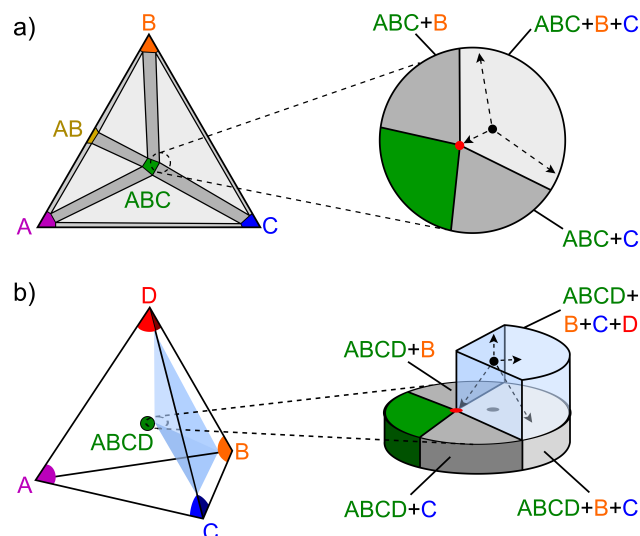

Fig. 1 Phase boundary mapping is a process that leverages the intentional synthesis in multi-phase regimes to control defect energetics. To highlight the fundamental principles of phase boundary mapping, a schematic (a) ternary and (b) quaternary diagram are used. For dilute impurities, synthesis in the multi-phase regime (black dot) produces samples with the matrix phase (ABC or ABCD) tied to the c-invariant point (red points). Using the quaternary diagram as an example, repeating the synthesis for each unique three-phase or four-phase region creates a sample set that maps the vertices of the single-phase polyhedron.

culminates in a series of samples that probe each vertex of the single-phase polygon.

Transitioning to the quaternary phase diagram (Figure 1b), our goal is the same – to evaluate all c-invariant points formed by the single-phase ABCD polyhedron. The concepts introduced for the ternary diagram extend naturally to the quaternary. Our schematic phase diagram (Figure 1b) shows a magnified view of one c-invariant point in the ABCD-B-C-D Alkemade tetrahedron. Quaternary c-invariant points are formed where the single-phase ABCD touches the four-phase region (Figure 1b, red point). Synthesis within the four-phase region will collapse the composition of the ABCD matrix phase to the c-invariant point. The process is repeated for each Alkemade tetrahedron, which culminates in a series of samples that probes the vertices of the single-phase ABCD polyhedron.

To summarize, phase boundary mapping can be summarized into three actionable items:

  I Determine phase diagram surrounding the phase of interest
 II Characterize any unknown phases that emerge
III Synthesis and characterization of samples at all c-invariant points in the phase diagram

As outlined above, this work begins with the investigation of the Cu-Hg-Ge-Te phase diagram, identifying all Alkemade tetrahedra formed by $Cu_2HgGeTe_4$ and neighboring phases. In the process, we identify a new phase, Hg_2GeTe_4, which crystallizes in the defect-chalcopyrite structure. We discover that Hg_2GeTe_4 shares a full solid solution with $Cu_2HgGeTe_4$, demonstrating high off-stoichiometry between Cu and Hg within this system. Den-

sity functional theory (DFT) electronic structure calculations support the formation of an alloy and suggest that Hg_2GeTe_4 is also a good candidate thermoelectric. Enabled by the high degree of off-stoichiometry between Cu and Hg, we find that we can manipulate the carrier density within the Hg_2GeTe_4-$Cu_2HgGeTe_4$ system between the intrinsic ($<10^{17}$ h$^+$cm^{-3}) and degenerate ($>10^{21}$ h$^+$cm^{-3}) regimes *via* rational changes in the c-invariant point composition. This work represents a critical step towards the realization of n-type transport in the $Cu_2HgGeTe_4$ system and further demonstrates the power of phase boundary mapping in complex systems.

2 Methods

2.1 Experimental

All powders and polycrystalline ingots were synthesized through solid state methods. All milling, sieving, and handling of powders was performed in a nitrogen dry box with oxygen and water levels below 1 ppm. Appropriate ratios of elemental Cu (shot, Sigma 99.9%), Hg (liquid, Alfa 99.999%), Ge (ingot, Alfa 99.999%), and Te (ingot, Alfa 99.999%) were milled in tungsten carbide ball-mill vials with two 9/16" tungsten carbide balls for 90 min. Resulting powders were sieved through a 106 μm mesh, sealed within evacuated fused silica ampules and annealed at 350°C for >24 h. Resulting material is subsequently ground in an agate mortar, passed again through a 106 μm mesh and consolidated through uniaxial hot-pressing at 350°C and 40 MPa. Each sample is soaked at 350°C for an additional 18 h during consolidation. Samples were cooled at a rate <50°C/h to avoid quenching effects.

For phase diagram determination, each quaternary tetrahedron was probed by using the appropriate compositional basis vectors at 1:1:1:1 ratios. For example, to probe an Alkemade tetrahedron where the endpoints are suspected to be Ge + GeTe + Cu_2Te + $Cu_2HgGeTe_4$, the 1:1:1:1 composition was found by equal combination of the normalized basis vectors (e.g. xGe + x(1/2)GeTe + x(1/3)Cu_2Te + x(1/8)$Cu_2HgGeTe_4$). Assuming x=0.25 for each constituent, the mixture used to probe Ge-GeTe-Cu_2Te-$Cu_2HgGeTe_4$ would be $Cu_{0.23}Hg_{0.03}Ge_{0.41}Te_{0.33}$.

Once the phase diagram was defined, more precise samples with trace impurities (e.g. 3 vol.% each of Ge, GeTe, and Cu_2Te) were synthesized. This step is critical to reduce the influence of effective media corrections. It is particularly important to note phases with severe off-stoichiometry, as they will offset the basis vectors used during synthesis. For example, consider the Cu_2GeTe_3-$Cu_{1.4}Te$-Cu_2Te-$Cu_2HgGeTe_4$ c-invariant point. The integration of Hg into Cu_2GeTe_3 and excess Cu into $Cu_2HgGeTe_4$ shifts the successful sample stoichiometry to a mixture of 23 mol% Cu_2GeTe_3, 10 mol% $Cu_{1.4}Te$, 13 mol%CuTe, and 54 mol% $Cu_2HgGeTe_4$.

Phase determination and lattice parameter analysis was performed for every sample using a combination of X-ray diffraction (XRD), scanning electron microscopy (SEM), and energy dispersive spectroscopy (EDS). Diffraction studies were performed on a Bruker D2 Phaser diffractometer in θ-2θ mode from 10 to 80° of 2θ. Resulting patterns were analyzed *via* Rietveld and Paw-

ley refinement using the Topas Academic V6 software package.[54] Detailed microscopy was performed on a JEOL JSM-7000F Field Emission SEM. Energy dispersive spectroscopy studies were performed on a FEI Quanta 600i Environmental SEM.

For the structure determination of Hg_2GeTe_4, a pure sample was sieved through a 50 μm mesh and diluted with amorphous SiO_2 to reduce X-ray absorption. The sample was sealed under nitrogen into a kapton capillary tube and measured at the Advanced Photon Source 11-BM beamline with 0.412725Å radiation. Discrete detectors covering an angular range from -6 to 16 degrees of 2θ were scanned over a 34 degree range, with data points collected every 0.001° with a scan speed of 0.01°/s. Charge flipping structure solution and subsequent Rietveld analysis was performed using Topas Academic V6 using the method pioneered by Oszlanyi and Suto, implemented by Coelho.[54–57]

Hall effect and resistivity measurements were performed using the Van der Pauw geometry on a home-built apparatus. Measurements were conducted up to 250°C under dynamic vacuum ($<10^{-5}$ Torr) with pressure-assisted, nichrome wire contacts. To allow contact annealing, samples undergo one thermal cycle before transport data is taken. Seebeck coefficient measurements were conducted using the quasi-steady slope method to 250°C under high vacuum ($<10^{-6}$Torr). Thermal diffusivity was measured using a Netzsch Laser Flash Apparatus (LFA) 457 and the resulting diffusivity data fit using a Cowen plus Pulse Correction (CPC) numerical model. The heat capacity is estimated using the Dulong-Petit approximation.

2.2 Computation

Density functional theory (DFT) is used to calculate the electronic band structure and the electron localization function (ELF) of Hg_2GeTe_4 and $Cu_2GeHgTe_4$. The employed first-principles approach is based on the Kohn-Sham DFT (KS-DFT),[58] as implemented in the Vienna ab initio simulation package (VASP).[59,60] The core and valence electrons are treated with the projector-augmented wave (PAW) method.[61] The Kohn-Sham orbitals are expanded in a plane-wave basis with a cutoff energy of 550eV. A Gamma-centered 4×4×4 grid is used to sample the Brillouin zone (BZ), following the scheme proposed by Monkhorst-Pack.[62] A finer 6×6×6 grid is used to ensure that convergence is achieved. Visualization of the ELFs were achieved with an electron isosurface cutoff of 0.886.

Structural optimization is performed with a tolerance of 0.001 eV/Å. The HSE06 hybrid exchange-correlation functional is used to estimate the electronic structure.[63,64] This gives a better description of the band gap, which is well known to be underestimated by standard DFT exchange-correlation functionals.

3 Results and Discussion

As outlined in the introduction, this work is organized into three sections, each providing key insight into the process of phase boundary mapping in a complex system like $Cu_2HgGeTe_4$:

I Determination of the Cu-Hg-Ge-Te phase diagram from a combination of experimental efforts and literature meta-analysis.
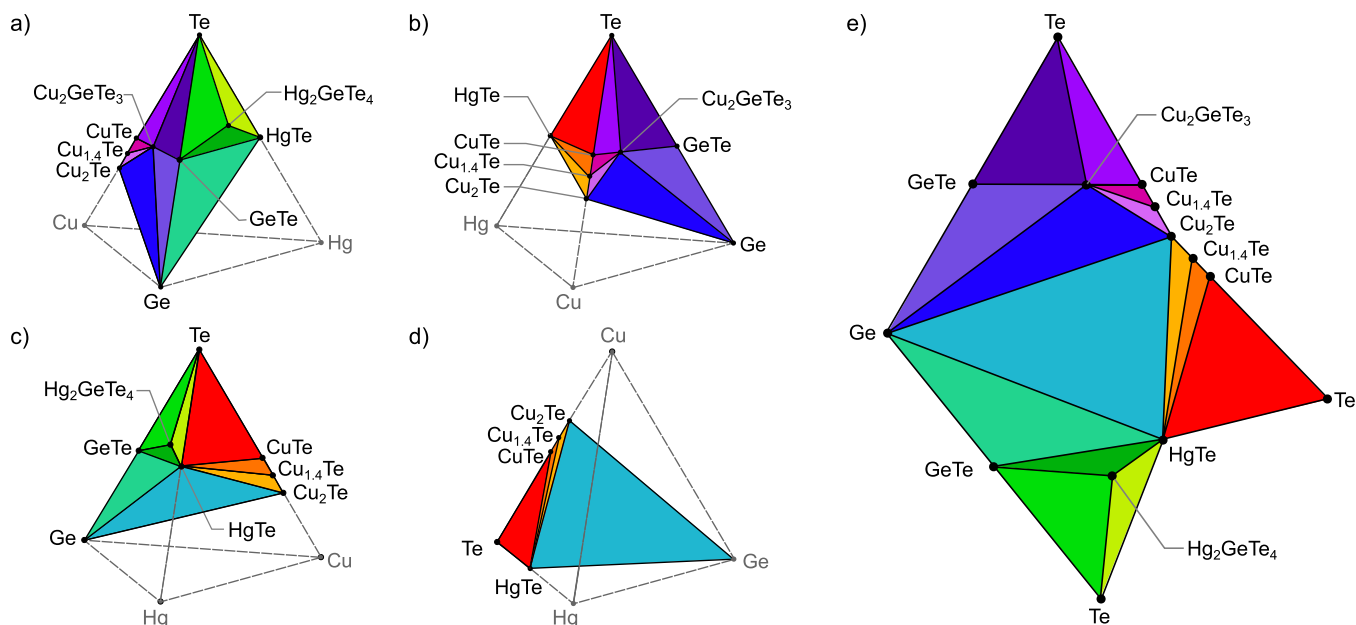
Fig. 2 Shown are four isometric projections (a-d) of the experimentally determined phase diagram under our process conditions (300 °C). For clarity, $Cu_2HgGeTe_4$ is not shown, but can be presumed to exist in equilibrium with every colored tetrahedra. To obtain a more transparent representation of the data, we can transform the 3-dimensional phase diagram by "unfolding" the colored volume (e). As $Cu_2HgGeTe_4$ is the only quaternary compound in the volume, we obtain a 2-dimensional representation of the phase diagram where each colored region is also in equilibrium with $Cu_2HgGeTe_4$.

II Characterization of the newly discovered phase Hg_2GeTe_4 and its relation to $Cu_2HgGeTe_4$.

III Synthesis and measurement of transport properties at c-invariant points and interpretation within phase boundary mapping framework.

Our primary goal is to enable precise control over the carrier density in $Cu_2HgGeTe_4$. However, we also aim to prove the efficacy of phase boundary mapping as an elegant, purely experimental technique for probing the effect of chemistry on transport in complex systems.

3.1 Phase Diagram Determination

As is the case for many quaternary compounds, full knowledge of the Cu-Hg-Ge-Te phase diagram does not exist. To provide a reasonable scaffold for our work, we begin with a meta-analysis of the binary and pseudo-binary literature. We will consider only phases which are stable in the temperature range from room temperature to 350°C. As noted in our prior work, the maximum operating temperature for $Cu_2HgGeTe_4$ is likely below 300°C, so this is a reasonable restraint.

Fortunately, all six binary edges of the Cu-Hg-Ge-Te phase diagram are available in the literature. The Hg-Ge[65] and Cu-Hg[66] diagrams are devoid of any stable compounds within our temperature range. The Ge-Te,[67,68] Hg-Te,[69,70] and Cu-Ge[71,72] diagrams reveal the presence of the binary compounds GeTe, HgTe, Cu_3Ge, and $Cu_{17}Ge_3$. The Cu-Te diagram is worth noting separately – all sources point to a complex diagram rich with high-temperature phase transitions and off-stoichiometry.[73–75] Existing diagrams do not fully agree on the nature of the phase transformations, the associated temperatures, compositions, or structures. Near ambient conditions, however, most sources agree that

there are three relatively well-defined binary compounds: CuTe, $Cu_{1.4}Te$, and Cu_2Te.[73–75]

Pseudo-binary and ternary data exists sporadically within the Cu-Hg-Ge-Te system. The most detailed work was performed within the Cu-Ge-Te ternary face and reveals the presence of Cu_2GeTe_3.[76] A later study for the Cu_2GeTe_3-HgTe pseudo-binary reveals a surprising solubility of Hg in Cu_2GeTe_3 and also demonstrates the first evidence of off-stoichiometry in $Cu_2HgGeTe_4$.[77] No information is available for the Cu-Hg-Ge, Cu-Hg-Te, or Hg-Ge-Te ternary spaces.

The meta-analysis provided several key pieces of information: 1) all binary compounds are known, 2) off-stoichiometry should be expected for multiple phases, and 3) when investigating faces/volumes where no literature exists, care should be taken to watch for the emergence of new compounds. Following the procedure outlined in the Methods section, we surveyed the Cu-Hg-Ge-Te phase space – the result is shown in Figure 2

As the quaternary diagram at a given temperature is a three-dimensional object, we have shown four isometric projections of the diagram in Figures 2a–d. For graphical clarity, $Cu_2HgGeTe_4$ is not shown; however, as the only quaternary compound that we observe, it coexists with any colored region. Figure 2d shows that the Ge-HgTe-Cu_2Te-$Cu_2HgGeTe_4$ Alkemade tetrahedron prevents the quaternary composition from ever being in equilibrium with Cu, Hg, Cu_3Ge, $Cu_{17}Ge_3$, or any unknown phases in the Cu-Hg-Ge ternary face. Regions of the phase diagram not in equilibrium with $Cu_2HgGeTe_4$ are irrelevant from a phase boundary mapping perspective and are not investigated further. This is actually quite fortunate, as it is infeasible to synthesize samples in equilibrium with elemental Hg. In practice, any phase diagram containing an element in a different physical state of matter (e.g. O_2, N_2, Hg) in

equilibrium with the phase of interest may require modifications to the phase boundary mapping procedure.

The compound Hg_2GeTe_4 is not reported in any known phase diagram or crystallographic database. To our knowledge, this work is the first report of Hg_2GeTe_4. Unlike all other relevant phases in Figure 2, Hg_2GeTe_4 and $Cu_2HgGeTe_4$ do not share a four-phase region. In fact, any attempts to synthesize samples within the larger region bound by Te-HgTe-GeTe-$Cu_2HgGeTe_4$ (in which Hg_2GeTe_4 is contained), yields three-phase samples. Our discovery of the full-solid solution between Hg_2GeTe_4 and $Cu_2HgGeTe_4$ ultimately explains the anomaly. The alloy has a profound effect on the single-phase region of $Cu_2HgGeTe_4$ and is discussed in detail later.

The isometric projections of the phase diagram shown in Figure 2a–d do not facilitate a discussion of changes in transport or crystallography as a function of c-invariant point composition. As such, we present a two-dimensional variation of the quaternary phase diagram, shown in Figure 2e. To obtain Figure 2e from Figure 2a, we first isolate the relevant Alkemade tetrahedra (those which have $Cu_2HgGeTe_4$ as a vertex). As $Cu_2HgGeTe_4$ is the only quaternary composition within the diagram, we can treat the colored volume as a projection of the Alkemade tetrahedra onto the faces of an irregular tetrahedra. Finally, we can "unfold" the tetrahedron to obtain a two-dimensional representation of the diagram. In this representation, we will use each colored triangle in Figure 2e to represent a singular c-invariant point (a vertex on the $Cu_2HgGeTe_4$ single-phase polyhedron). For example, the red triangle bound by CuTe-HgTe-Te on Figure 2e represents the c-invariant point of $Cu_2HgGeTe_4$ that is formed by the intersection of the $Cu_2HgGeTe_4$ single phase region and the four-phase alkemade tetrahedron $Cu_2HgGeTe_4$-CuTe-HgTe-Te (recall the discussion surrounding Figure 1b).

We previously alluded to a full solid solution between Hg_2GeTe_4 and $Cu_2HgGeTe_4$. The presence of this alloy precludes the formation of a true four-phase region in any sample containing the Hg_2GeTe_4-$Cu_2HgGeTe_4$ solid solution. This region plays a critical role in our ability to manipulate the carrier density within the $Cu_2HgGeTe_4$ system. As a result, we find it instructive to pause and focus on Hg_2GeTe_4 and the solid solution with $Cu_2HgGeTe_4$.

3.2 The Hg_2GeTe_4-$Cu_2HgGeTe_4$ solid solution

While mapping the Hg-rich side of the Cu-Hg-Ge-Te phase diagram, we noted that $Cu_2HgGeTe_4$ exhibited an unusual degree of off-stoichiometry, allowing Hg to readily substitute for Cu. We hypothesized that $Cu_2HgGeTe_4$ was alloying with an unknown phase on the Hg-Ge-Te face of the diagram. Synthesis on the Hg-Ge-Te ternary face revealed the compound Hg_2GeTe_4, for which no prior information was available. A powder sample of Hg_2GeTe_4 was measured at the Advanced Photon Source at Argonne National Laboratory (BM-11) using high-resolution synchrotron X-ray diffraction. From the resulting diffraction pattern (ESI Figure S1), we performed ab-inito structure solution via the method of charge flipping.[54–57] The structure is shown in Figure 3 alongside $Cu_2HgGeTe_4$.

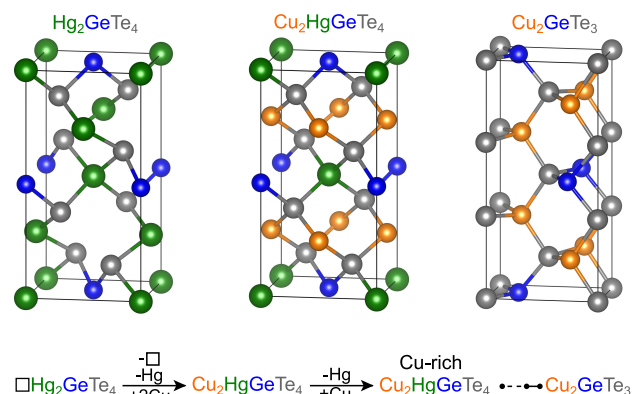Fig. 3 The newly discovered ternary compound Hg_2GeTe_4 crystallizes in the defect chalcopyrite structure. Our analysis indicates that Hg_2GeTe_4 and $Cu_2HgGeTe_4$ share a full solid solution. Significant off-stoichiometry is noted on the Cu-rich side of $Cu_2HgGeTe_4$. A Cu-rich diamond-like semiconductor (Cu_2GeTe_3) exists as well, although it does not share a full solution with $Cu_2HgGeTe_4$. The facile swapping of Hg and Cu is surprising, although transitions between each structure are well modeled by considering Hg_{Cu} and Cu_{Hg} substitution – simple reaction schema are shown to highlight this point.

The structure of Hg_2GeTe_4 is consistent with the defect chalcopyrite prototype (e.g. $CdGa_2Se_4$,[78,79] $HgGa_2Se_4$,[79] and $ZnGa_2Se_4$[80]) Our analysis suggests that the vacancies within Hg_2GeTe_4 are ordered. All Ge and Hg cations are tetrahedrally coordinated by Te. However, we note that the constituent tetrahedra are relatively distorted. Visual comparison with $Cu_2HgGeTe_4$ shows the striking similarity between the two structures and supports the formation of an alloy.

To highlight the structure and connection to the quaternary composition, Hg_2GeTe_4 can be written explicitly as a vacancy structure $\Box Hg_2GeTe_4$ where $\Box$ in Figure 3 indicates the vacant cation sites. Assuming that Hg exists as Hg^{2+} in Hg_2GeTe_4 and that Cu integrates as Cu^{1+}, charge balance can be maintained by exchanging Cu and Hg at a 2:1 ratio. This is envisioned as the creation of one Cu_{Hg} defect and the simultaneous annihilation of a vacancy. Cu substitution can be continued in this manner until the stoichiometry reaches the nominal composition of the stannite $Cu_2HgGeTe_4$ structure. In principle, either Hg site could be involved in Cu_{Hg} defect formation. However, examining the stannite $Cu_2HgGeTe_4$ structure, we note that the Cu atoms nominally exist on planes at $z = 1/4$ and $z = 3/4$. Noting that the vacant cation sites in Hg_2GeTe_4 also exist within planes at $z = 1/4$ and $z = 3/4$, we hypothesize that the substitution of Cu may occur preferentially on these layers. A more detailed crystallographic study is underway to identify the exact nature of the Cu substitution.

As noted in prior literature studies, $Cu_2HgGeTe_4$ also appears to exhibit off-stoichiometry in the Cu-rich direction.[77] However, as there are no more vacant sites in $Cu_2HgGeTe_4$, additional substitution of Cu on Hg must occur at a 1:1 ratio. In the absence of additional compensating defects (e.g. anion vacancies) this reaction should create an excess of free holes. The substitution of Cu for Hg in $Cu_2HgGeTe_4$ pushes the composition towards the Cu-Ge-Te face and the diamond-like compound Cu_2GeTe_3, shown in Figure
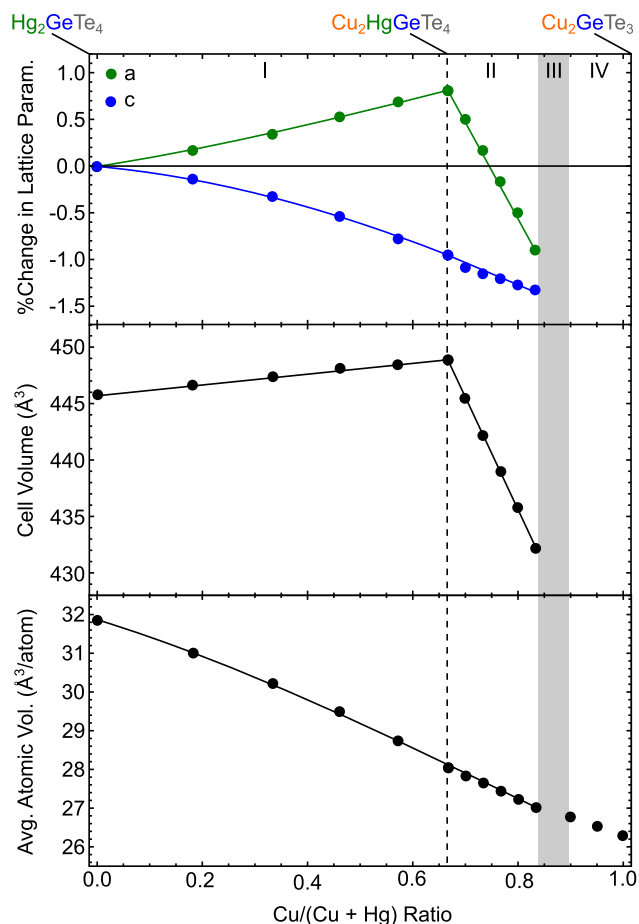
Fig. 4 Continuous changes in the lattice parameters and the cell volume as a function of Cu/Cu+Hg ratio indicate that Hg_2GeTe_4 and $Cu_2HgGeTe_4$ share a full solid solution (region I). A significant amount of excess Cu can be integrated into $Cu_2HgGeTe_4$ as Cu_{Hg} (region II) before termination of solid solution occurs around $Cu_{2.5}Hg_{0.5}GeTe_4$ (region III). We note that Cu_2GeTe_3 will incorporate a significant amount of Hg (region IV), consistent with literature results. Changes in slope within region I and II can be rationalized by considering the competing effects of Cu_{Hg} substitution versus vacancy annihilation. Solid black lines serve as guides to the eye within the single-phase alloy.

3. Our phase analysis, however, indicates that $Cu_2HgGeTe_4$ and Cu_2GeTe_3 do not share a full solid solution.

To highlight the properties and structure of the Hg_2GeTe_4-$Cu_2HgGeTe_4$ alloy we synthesized several intermediate compositions. For completion, we also examined the Cu-rich compositions between $Cu_2HgGeTe_4$ and Cu_2GeTe_3. Figure 4 summarizes the lattice parameters, cell volume, and average atomic volume for each sample as a function of Cu/Cu+Hg ratio. We can broadly divide Figure 4 into four main regimes:

  I Alloying between Hg_2GeTe_4 and $Cu_2HgGeTe_4$
  II Excess integration of Cu into $Cu_2HgGeTe_4$
  III Solubility gap between $Cu_2HgGeTe_4$ and Cu_2GeTe_3
  IV Integration of Hg into Cu_2GeTe_3

Focusing on region I, we first note linear changes in the lattice parameters, cell volume, and average atomic volume, consistent with alloying. These results indicate that there exists a *full solid solution* between Hg_2GeTe_4 and $Cu_2HgGeTe_4$. This is a relatively

profound observation – this has not been shown in any other quaternary diamond-like system. Note that the cell volume weakly increases with the incorporation of Cu into Hg_2GeTe_4 until the nominal stoichiometry of $Cu_2HgGeTe_4$ is reached. There are two competing effects at play here: 1) a volumetric expansion due to annihilation of vacant sites and 2) a volumetric compression due to the Cu_{Hg} substitution.

To first order, we can motivate the changes in the *a* and *c* lattice parameters through simple geometric arguments. Consider modeling Hg_2GeTe_4 as constructed from cation-centered tetrahedra arranged. For this argument, consider the vacancy centers as "cation-centers" as well. The base of the tetrahedral cell has a hypotenuse whose length is the sum of a vacancy-centered tetrahedron and a Hg-centered tetrahedron. When transitioning to $Cu_2HgGeTe_4$, we replace both with Cu-centered tetrahedra. When we compare the relative dimensions of the vacancy-centered tetrahedron and the Hg-centered tetrahedra (from Hg_2GeTe_4) with Cu-centered tetrahedra (from $Cu_2HgGeTe_4$), we find that the expansion of the vacancy site outweighs the compression of the Hg site. Thus, consistent with the experimental data, the incorporation of Cu into Hg_2GeTe_4 actually expands *a*.

For the contraction in *c*, there is a simpler, conceptual approach. As shown in Figure 3, let us consider Hg_2GeTe_4 as built of slabs of atoms normal to the c-direction (e.g. Hg-Ge at $z = 0$, Te at $z = 1/8$, Hg-□ at $z = 1/4$...). If we consider Te as residing in a rigid layer, the distance between the Te-Te slabs will be set by the largest interlayer cation. To first order, the separation of all Te-Te layers is set entirely by the Hg atoms. Substitution of Cu onto a vacancy site in this regime will not cause an expansion in *c*, although substitution of Cu_{Hg} will decrease the average Te-Te slab separation. Thus, we could reasonably expect a net contraction in *c* with Cu integration.

We now turn to region II, where we observe a sharp decrease in *a* and the cell volume. There are no more vacancy sites, so all addition of Cu occurs as Cu_{Hg} defects. Our previous model balanced the expansive and compressive effects of Cu integration using tetrahedral building blocks. Without the expansive effect of vacancy-filling, we now observe the strong contraction from Cu_{Hg} – thus the sharp decrease in *a*. As for *c*, we argued that the Hg atoms determine the Te-Te slab distance. The argument did not require any consideration of the vacancy sites. Thus, substitution of Cu for Hg in region II is not fundamentally different from region I as far as *c* is concerned.

Within regions III and IV, we observe the termination of solid-solubility at a Cu-rich composition of approximately $Cu_{2.5}Hg_{0.5}GeTe_4$. On the other side of the solubility gap, we observe that Cu_2GeTe_3 integrates a significant amount of Hg as Hg_{Cu} defects with a termination of solid-solubility at approximately $Cu_{1.8}Hg_{0.2}GeTe_3$. The extent of Hg integration into Cu_2GeTe_3 is consistent with prior literature.[77]

Unlike the lattice parameters and cell volume, the average atomic volume is remarkably linear throughout the entire region. We performed some basic modeling of the effect of Cu substitution (compression and expansion) along with the effect of varying number of atoms (e.g. 14 in Hg_2GeTe_4, 16 in $Cu_2HgGeTe_4$).
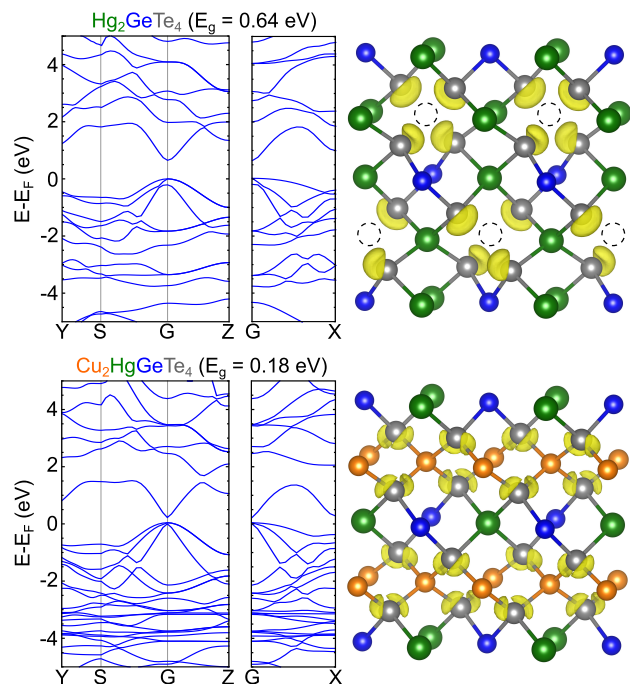
Fig. 5 The electronic structures of Hg_2GeTe_4 and $Cu_2HgGeTe_4$ are remarkably similar, consistent with the formation of an alloy. We note, however, that Hg_2GeTe_4 possesses a significantly larger band gap. The electron localization functions (right) help visualize the most localized electrons in each system. As expected from charge counting arguments, Hg_2GeTe_4 exhibits lone-pair electrons oriented towards the vacant cation sites.

Our results indicate that linearity is not a general result, but is a mathematical coincidence. The linearity is a peculiar alignment of multiple effects: 1) the similarity between the magnitude of the compressive Cu_{Hg} and expansive vacancy annihilation, and 2) the renormalization per number of atoms per unit cell. A subtle non-linearity in region I, however, can be traced to the changing number of atoms per formula unit and the corresponding normalization. The persistence of the trend through the solubility gap is intriguing. However, as all three materials are diamond-like tellurides, the changes in average atomic volume are analogous to the average cation radius, which should smoothly track changes in composition.

Our high-throughput computational survey suggested that $Cu_2HgGeTe_4$ showed promise as an n-type material due to desirable electronic properties within the conduction band.[5] We were interested to see how the fundamental electronic structures of Hg_2GeTe_4 compares with $Cu_2HgGeTe_4$. As there is an alloy between the two structures, we need to be cognizant of changes in the electronic structure that could significantly disrupt the electronic transport. Figure 5 presents the calculated band diagrams for Hg_2GeTe_4 and $Cu_2HgGeTe_4$ alongside the electronic localization functions (ELFs) for each structure.

The general features of the electronic structure for $Cu_2HgGeTe_4$ are relatively unperturbed as we transition to Hg_2GeTe_4. However, we note a significant increase in the DFT band gap of Hg_2GeTe_4 (0.64 eV) when compared to $Cu_2HgGeTe_4$ (0.18 eV). This effect is likely similar to the anomalous increase in the band

gap observed between some binary II-VI (e.g. ZnSe, 1.32 eV) materials versus the analogous I_B-III-VI_2 materials (e.g. $CuGaSe_2$, 1.81 eV).[14,81,82] In $Cu_2HgGeTe_4$, the top of the valence bands are formed from Te 5p and Cu 3d anti-bonding states. Moving deeper into the bands, we encounter Cu 3d non-bonding states and then finally Te 5p/Cu 3d bonding states. The interaction between the non-bonding Cu 3d states and the anti-bonding Te 5p/Cu 3d states yields a repulsive p-d interaction that increases the energy of the anti-bonding states and subsequently reduces the band gap. Besides the increased band gap, however, the general features of the electronic structure (particularly for n-type transport) in Hg_2GeTe_4 mimic $Cu_2HgGeTe_4$ quite well.

We can also examine the electron localization function (ELF) to gain insight into the real space distribution of the most localized electrons in the structure. Figure 5 shows the respective electron densities. Both structures show localization of electrons on the Te atoms. The ELF for Hg_2GeTe_4 is particularly interesting, however, as we can observe Te lone-pair electrons oriented towards the vacant cation sites. In $Cu_2HgGeTe_4$, the most localized electrons remain on Te, but the effective electron density is split between the neighboring Cu atoms. This behavior suggests that bonding between Cu and Te in $Cu_2HgGeTe_4$ is likely polar-covalent with a sizable (though incomplete) charge transfer from Cu to Te.

To first order, the electronic properties of n-type Hg_2GeTe_4 should mimic those predicted for $Cu_2HgGeTe_4$. Our experimental results confirm the presence of a full-solid solution between Hg_2GeTe_4-$Cu_2HgGeTe_4$, highlighting an unusual affinity for Hg_{Cu} and Cu_{Hg} substitution. The high degrees of off-stoichiometry make $Cu_2HgGeTe_4$ a particularly interesting candidate for phase boundary mapping.

3.3 Phase Boundary Mapping Results

With the phase diagram well-characterized, we proceeded to synthesize the c-invariant points using the techniques outlined in the Methods section. Each c-invariant point was confirmed using a mixture of X-ray diffraction and microscopy – all SEM, XRD, and EDS results can be found in the ESI Figures S2-15. Consistent with the Hg_2GeTe_4-$Cu_2HgGeTe_4$ solid solution, we continue to observe high degrees of off-stoichiometry in the Hg and Cu directions. Some deviation is noted in the Ge and Te directions, although the single-phase region appears to be largely needle-like, extending from Hg_2GeTe_4 through $Cu_2HgGeTe_4$, and nearly reaching Cu_2GeTe_3.

The needle-like nature of the single-phase region naturally pushed us towards investigating off-stoichiometry along the Cu-rich and Hg-rich directions (e.g. Figure 4). In general, however, we are not guaranteed that the Ge and Te directions do not play a role in the defect energetics of $Cu_2HgGeTe_4$. In the absence of computation, there are uncountably many compositional studies that could be constructed to probe the single-phase region. Within the framework of phase boundary mapping, however, there are a finite number of well-defined c-invariant points (14 for $Cu_2HgGeTe_4$) that serve to probe all constituent chemical potential extrema within the single-phase region. To elucidate this point, Figure 6 investigates the changes in the average atomic
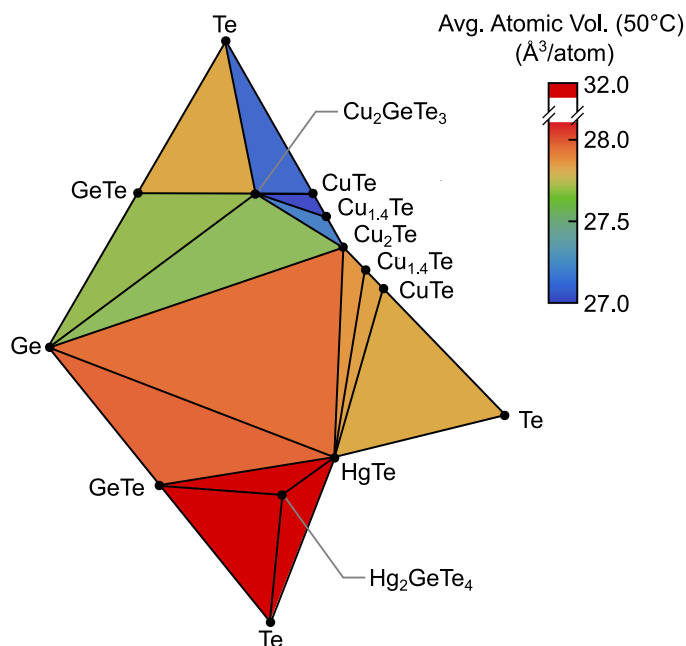
Fig. 6 Projection of the average atomic volume onto our phase diagram reveals a strong volumetric contraction towards the Cu-rich c-invariant points. As the c-invariant points related to Hg_2GeTe_4 are formally three-phase and lie upon the HgTe-GeTe-Te ternary face, they are compositionally distant from the bulk of the single-phase region (note the large volume change and discontinuous scale). However, as seen previously in Figure 4, the alloy demonstrates a smoothly varying average atomic volume as we transition from Hg_2GeTe_4 to $Cu_2HgGeTe_4$.

Fig. 7 Projection of the carrier density on our c-invariant point phase diagram reveals a wide range of achievable carrier densities depending on the composition. Consistent with the creation of Cu_{Hg}^- defects, degenerate carrier densities in excess of 10^{21} h$^+$cm^{-3} are observed in Cu-rich regions. Inversely, c-invariant points associated with the Hg_2GeTe_4-rich end of the Hg_2GeTe_4-$Cu_2HgGeTe_4$ alloy exhibit intrinsic transport with carrier densities on the order of 10^{17} h$^+$cm^{-3}. We find the decrease in carrier concentration near Hg_2GeTe_4 intriguing, as the charge-balanced substitution of 2:1 Cu^{1+} for Hg^{2+} is not expected to change the carrier density.

volume as a function of c-invariant point composition. This is analogous to the Vegard's Law study shown in Figure 4, although phase boundary mapping investigates the entire single-phase region without bias or the need to confine the study to a single dimension (e.g. Cu/Cu+Hg). As the c-invariant points probe the *extrema* of the single-phase region, and due to the presence of the Hg_2GeTe_4-$Cu_2HgGeTe_4$ alloy, the scale is discontinuous near the Hg_2GeTe_4 region.

Alongside Figure 4, this completes the crystallographic survey of the single-phase region. Consistent with our alloying study, we see a relatively continuous decrease in the average atomic volume as we approach the Cu-rich side of the phase diagram. While it appears as though the region connecting Hg_2GeTe_4 with the other four-phase c-invariant points is discontinuous with the rest of the map, recall that the average atomic volume (Figure 4) connects linearly with the nominal $Cu_2HgGeTe_4$ composition. Graphically, the stark difference occurs because the c-invariant points near Hg_2GeTe_4 formally probe the three-phase c-invariant points between the Hg_2GeTe_4-$Cu_2HgGeTe_4$ single-phase region and the Hg-Ge-Te face, which are compositionally distant from the bulk of the quaternary c-invariant points. The large change in average atomic volume throughout the phase diagram is a key result, as it highlights the breadth of compositional change between c-invariant points. Next we examine the influence of the chemical changes on the carrier densities – the crux of phase boundary mapping.

Figure 7 presents the results of Hall carrier concentration mea-
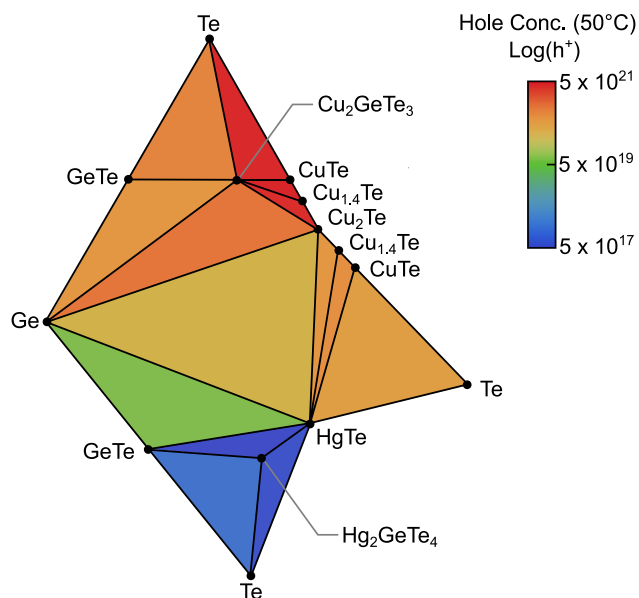
surements at the relevant c-invariant points. Consistent with the large degree of off-stoichiometry in $Cu_2HgGeTe_4$, we see a dramatic spread in the carrier density between c-invariant points. Cu-rich compositions in equilibrium with the ternary Cu_2GeTe_3 show the most degenerate compositions, with hole densities in excess of 10^{21} h$^+$cm^{-3}. Hg-rich compositions, in particular Hg_2GeTe_4, show the most intrinsic compositions, with hole densities on the order of 10^{17} h$^+$cm^{-3}. With this range of compositions, optimization for p-type transport should be readily obtainable within the single-phase volume. Furthermore, as the Hg_2GeTe_4 alloy enables intrinsic transport, we have also managed to find a composition amenable to n-type extrinsic doping. Use of Hg_2GeTe_4 may allow extrinsic studies to avoid the influence of energetically favorable defects that normally force Cu-rich compositions to exhibit p-type transport.

Beginning with the Cu-rich region, we previously proposed that the substitution of excess Cu^{1+} into the nominal $Cu_2HgGeTe_4$ structure occurs at a 1:1 ratio as Cu_{Hg}^- defects (Figure 4, region II). The creation of free holes with excess Cu integration is intuitive and matches the general trends we observe in Figure 7. However, we acknowledge that the underlying defect structures are likely more complex and probably involve contributions from all of the constituent elements. Nevertheless, to first order, our model does not take into account compensating defects (e.g. V_{Te}^{2+}), defect clusters, or changes in oxidation state. For the $Cu_2HgGeTe_4$ system, however, off-stoichiometry in the Ge and Te directions pales in comparison to the flexibility of the Cu and Hg

sites. We find it reasonable to assume that the dominant defect is likely related to the Cu/Cu+Hg ratio. Furthermore, the experimental XRD and Hall Effect measurements appear to corroborate a underlying defect structure with strong ties to Cu and Hg.

As we transition between $Cu_2HgGeTe_4$ and Hg_2GeTe_4 (Figure 4, region I), our proposed substitution schema are charge-balanced. A substitution of 2 Cu^{1+} for a Hg^{2+} and a neutral vacancy is not expected to significantly change the charge carrier density. Our EDS and XRD results (ESI Figures 13-15) confirm that the single-phase region for Hg_2GeTe_4-$Cu_2HgGeTe_4$ alloy is quite narrow in the Ge and Te directions, suggesting that the charge-balanced substitution is well adhered to. Furthermore, there doesn't seem to be a large difference between the three c-invariant points on the HgTe-GeTe-Te face. All Cu-free compositions exhibit nearly identical charge carrier densities, consistent with a small degree of off-stoichiometry involving Hg, Ge and Te.

Speculating, we see several possible resolutions to the carrier density change along the Hg_2GeTe_4-$Cu_2HgGeTe_4$ alloy. Firstly, it is possible that the significant increase in the band gap towards Hg_2GeTe_4 changes the relative energy of the dominant defect relative to the band edges. Secondly, it is possible that the "nominal" composition for $Cu_2HgGeTe_4$ actually lies outside the single-phase volume (e.g. $Cu_2HgGeTe_4$ is destined to be "off-stoichiometric" at all compositions). This could potentially explain the transition to intrinsic behavior as the compound alloys with Hg_2GeTe_4 – we traverse a line in the phase diagram that starts at an off-stoichiometric composition ($Cu_2HgGeTe_4$), but which ends in a charge-balanced regime by Hg_2GeTe_4. In this case, it is likely more accurate to refer to Hg_2GeTe_4 as the parent structure and $Cu_2HgGeTe_4$ as the defect structure. We see these types of questions as examples where synergy between phase boundary mapping and computation would yield insightful results.

To further probe the nature of the carrier density decrease along the Hg_2GeTe_4-$Cu_2HgGeTe_4$ alloy, we synthesized samples of $Cu_{2x}Hg_{2-x}GeTe_4$ (x = 0, 0.2, 0.4, 0.6, 0.8, 1.0). Phase boundary mapping is not routinely applied within alloys – however the concept extends naturally by synthesizing the alloyed samples with trace impurities of HgTe and GeTe. The impurities will pin the alloyed samples along a particular edge of the Hg_2GeTe_4-$Cu_2HgGeTe_4$ single-phase volume. To aid understanding, a schematic of this region is shown in Figure 8. Note that, unlike the other phase boundary mapping regions, these samples do not condense to a singular c-invariant point. The true c-invariant points for the single-phase region are formed by HgTe-GeTe-Hg_2GeTe_4, Te-HgTe-Hg_2GeTe_4, and Te-GeTe-Hg_2GeTe_4 as shown previously in Figure 7. We chose the region containing HgTe and GeTe because samples at the corresponding c-invariant point show the most intrinsic transport. Additional microscopy, diffraction, and composition results for the alloyed samples are shown in the ESI Figures 16-20.

Hall Effect measurements on the $Cu_{2x}Hg_{2-x}GeTe_4$ series of alloys confirm that the carrier density and electronic resistivity vary smoothly as we transition from degenerate $Cu_2HgGeTe_4$ to intrinsic Hg_2GeTe_4. Additional results highlighting the changes in lattice thermal conductivity and mobility with alloying are included
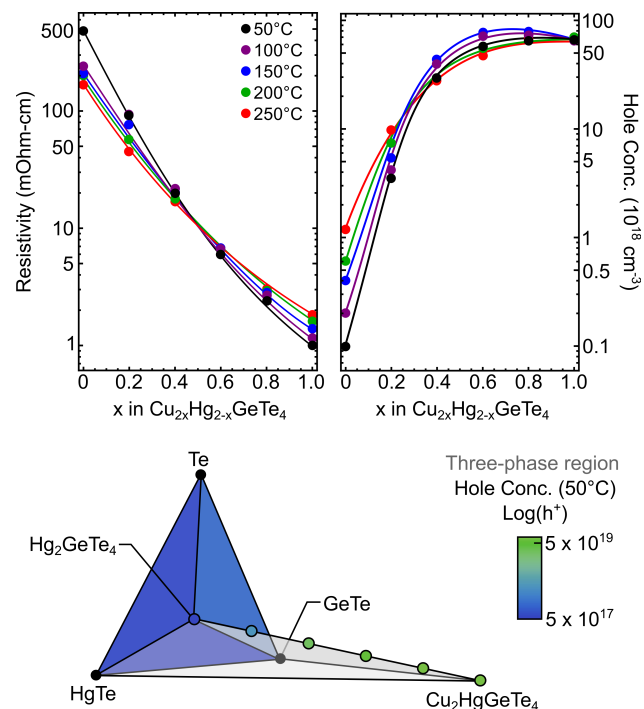

Fig. 8 Recall that the full solid solution between Hg_2GeTe_4-$Cu_2HgGeTe_4$ precludes the existence of a formal four-phase c-invariant point in the region bound by GeTe-HgGe-Te. As such, we investigate along the *edge* formed by GeTe-HgTe-$Cu_{2x}Hg_{2-x}GeTe_4$. We find that plots of the electronic resistivity and hole concentration vary smoothly with Cu integration. A schematic of the edge formed by the three-phase region is also shown with compositions colored to be consistent with the c-invariant point heat map shown in Figure 7. This result confirms full carrier density control from the degenerate to intrinsic regime.

in the ESI Figure 21. We observe strong alloy scattering in both the electronic and thermal transport, consistent with increased disorder as Cu integrates into Hg_2GeTe_4. This result confirms that we have complete control over the carrier density (10^{17} – 10^{21} h^+cm^{-3}) in the $Cu_2HgGeTe_4$ system by rationally varying the Cu/Cu+Hg content. While this work does not investigate the extrinsic n-type doping of Hg_2GeTe_4, we did perform a full suite of thermoelectric characterization on the p-type Hg_2GeTe_4-$Cu_2HgGeTe_4$ series of alloys. The results are included in the ESI Figure 22. As noted in ESI Figure 21, there is strong alloy scattering along the alloying series. The strong reduction of the mobility suggests that thermoelectric optimization would be better achieved by extrinsic p-type and n-type doping of Hg_2GeTe_4. It is also possible that the reduction in carrier concentration near the intrinsic regime is also reducing screening, enhancing scattering from charged defects. Note that the intrinsic nature of the Hg_2GeTe_4 samples prevents us from commenting about its ultimate thermoelectric efficiency, although additional doping work is ongoing.

While the extrinsic doping of Hg_2GeTe_4 is outside the scope of this work, our phase boundary mapping study has revealed a path for the realization of n-type transport in the Hg_2GeTe_4-$Cu_2HgGeTe_4$ system. Our study has allowed us to escape from the strongly degenerate Cu-rich compositions, reducing the influence

of energetically favorable p-type defects and enabling extrinsic studies. Furthermore, our work extended the concept of phase boundary mapping to alloys and proved the technique valuable even in exceedingly complex systems.

4 Conclusion

The optimization and application of new material systems is often hindered, sometimes fatally, by our inability to manipulate the carrier density. Our prior work on $Cu_2HgGeTe_4$ and related quaternary DLS revealed a schism between the experimentally realized carrier densities ($>10^{20}\,h^+cm^{-3}$) and our predictions of n-type thermoelectric performance. This work directly confronted the problem of doping in a complex system through application of the concept of phase boundary mapping.

Our work resulted in several critical results. We successfully created a phase diagram for the Cu-Hg-Ge-Te system, identifying all relevant composition-invariant points for the phase boundary mapping of $Cu_2HgGeTe_4$. During creation of the phase diagram, we discovered the ordered-vacancy structure Hg_2GeTe_4 and further discovered a full-solid solution between Hg_2GeTe_4 and $Cu_2HgGeTe_4$. We successfully synthesized samples at all relevant composition-invariant points, further extending the concept of phase boundary mapping along the Hg_2GeTe_4-$Cu_2HgGeTe_4$ alloy. Ultimately, our phase boundary mapping study revealed carrier density manipulation from intrinsic ($<10^{17}\,h^+cm^{-3}$) to degenerate ($>10^{21}\,h^+cm^{-3}$) through the engineering of native defects. By reducing the carrier density in the Hg_2GeTe_4-$Cu_2HgGeTe_4$ system to the intrinsic regime, we have enabled extrinsic doping as a means to realize n-type transport in future studies. Furthermore, we have demonstrated phase boundary mapping as a structured technique with the immense potential to augment the experimentalists' toolkit.

5 Conflicts of Interest

There are no conflicts of interest to declare.

6 Acknowledgements

References

1 H. Amano, M. Kito, K. Hiramatsu and I. Akasaki, *Jpn. J. Appl. Phys.*, 1989, **28**, L2112–L2214.

2 S. Nakamura, T. Mukai, M. Senoh and N. Iwasa, *Jpn. J. Appl. Phys.*, 1992, **31**, L139–L142.

3 J. Yan, P. Gorai, B. Ortiz, S. Miller, S. A. Barnett, T. Mason, V. Stevanović and E. S. Toberer, *Energy Environ. Sci.*, 2015, **8**, 983–994.

4 B. R. Ortiz, W. Peng, L. C. Gomes, P. Gorai, T. Zhu, D. M. Smiadak, G. J. Snyder, V. StevanoviĭÀ, E. Ertekin, A. Zevalkink and E. S. Toberer, *Chem. Mater.*, 2018, **30**, 3395–3409.

5 P. Gorai, D. Gao, B. Ortiz, S. Miller, S. A. Barnett, T. Mason,

6 S. Zhang, S.-H. Wei and A. Zunger, *J. Appl. Phys.*, 1998, **83**, 3192–3196.

7 W. Faschinger, *J. Cryst. Growth*, 1996, **159**, 221–228.

8 S. Lany and A. Zunger, *Model. Simul. Mater. Sci. Eng.*, 2009, **17**, 084002.

9 A. Zunger, *Appl. Phys. Lett.*, 2003, **83**, 57–59.

10 S.-H. Wei, *Comput. Mater. Sci.*, 2004, **30**, 337–348.

11 S. Zhang, S.-H. Wei and A. Zunger, *Phys. Rev. Lett.*, 2000, **84**, 1232–1235.

12 T. Maeda and T. Wada, *J. Phys. Chem. Solids*, 2005, **66**, 1924–1927.

13 S.-H. Wei, S. Zhang and A. Zunger, *Appl. Phys. Lett.*, 1998, **72**, 3199–3201.

14 S. Zhang, S.-H. Wei, A. Zunger and H. Katayama-Yoshida, *Phys. Rev. B*, 1998, **57**, 9642–9656.

15 S.-H. Wei, S. Zhang and A. Zunger, *J. Appl. Phys.*, 1999, **85**, 7214–7218.

16 L. Oikkonen, M. G. Ganchenkova, A. P. Seitsonen and R. Nieminen, *J. Phys. Condens. Matter*, 2011, **23**, 422202(1)–422202(5).

17 S.-H. Wei and S. Zhang, *J. Phys. Chem. Solids*, 2005, **66**, 1994–1999.

18 C. Domain, S. Laribi, S. Taunier and J. Guillemoles, *J. Phys. Chem. Solids*, 2003, **64**, 1657–1663.

19 L. Oikkonen, M. Ganchenkova, A. Seitsonen and R. Nieminen, *Journal of Physics: Condensed Matter*, 2014, **26**, 345501.

20 X. Sun, F. Jiang and J. Feng, *Comput. Mater. Sci.*, 2009, **47**, 31–34.

21 S. Chen, A. Walsh, J.-H. Yang, X.-G. Gong, L. Sun, P.-X. Yang, J.-H. Chu and S.-H. Wei, *Phys. Rev. B*, 2011, **83**, 125201(1)–125201(5).

22 Y.-T. Hsieh, Q. Han, C. Jiang, T.-B. Song, H. Chen, L. Meng, H. Zhou and Y. Yang, *Adv. Energy Mater.*, 2016, **6**, 1502386(1)–1502386(6).

23 S. Chen, J.-H. Yang, X.-G. Gong, A. Walsh and S.-H. Wei, *Phys. Rev. B*, 2010, **81**, 245204(1)–245204(10).

24 D. Mutter and S. T. Dunham, *IEEE J. Photovolt.*, 2015, **5**, 1188–1196.

25 S. Chen, A. Walsh, X.-G. Gong and S.-H. Wei, *Adv. Mater.*, 2013, **25**, 1522–1539.

26 S. Chen, L.-W. Wang, A. Walsh, X. Gong and S.-H. Wei, *Appl. Phys. Lett.*, 2012, **101**, 223901(1)–223901(4).

27 P. Zawadzki, A. Zakutayev and S. Lany, *Phys. Rev. B*, 2015, **92**, 201204(1)–201204(5).

28 V. Kosyak, N. Mortazavi Amiri, A. Postnikov and M. A. Scarpulla, *J. Appl. Phys.*, 2013, **114**, 124501(1)–124501(16).

29 D. Huang and C. Persson, *Thin Solid Films*, 2013, **535**, 265–269.

30 S. Chen, X. Gong, A. Walsh and S.-H. Wei, *Appl. Phys. Lett.*, 2010, **96**, 021902(1)–021902(3).

31 A. Nagoya, R. Asahi, R. Wahl and G. Kresse, *Phys. Rev. B*,

Q. Lv, V. Stevanović and E. S. Toberer, *Comput. Mater. Sci.*, 2016, **112**, 368–376.

2010, **81**, 113202(1)–113202(4).

32 T. Maeda, S. Nakamura and T. Wada, *Jpn. J. Appl. Phys.*, 2011, **50**, 04DP07(1)–04DP07(6).

33 N. Cheng, R. Liu, S. Bai, X. Shi and L. Chen, *J. Appl. Phys.*, 2014, **115**, 163705(1)–163705(7).

34 R. Liu, L. Xi, H. Liu, X. Shi, W. Zhang and L. Chen, *Chem. Commun.*, 2012, **48**, 3818–3820.

35 A. Kosuga, R. Higashine, T. Plirdpring, M. Matsuzawa, K. Kurosaki and S. Yamanaka, *Jpn. J. Appl. Phys.*, 2012, **51**, 121803(1)–121803(4).

36 A. Kosuga, T. Plirdpring, R. Higashine, M. Matsuzawa, K. Kurosaki and S. Yamanaka, *Appl. Phys. Lett.*, 2012, **100**, 042108(1)–042108(3).

37 A. Yusufu, K. Kurosaki, A. Kosuga, T. Sugahara, Y. Ohishi, H. Muta and S. Yamanaka, *Applied Physics Letters*, 2011, **99**, 061902.

38 H. Xie, X. Su, G. Zheng, T. Zhu, K. Yin, Y. Yan, C. Uher, M. G. Kanatzidis and X. Tang, *Adv. Energy Mater.*, 2017, **7**, 1601299(1)–1601299(14).

39 Y. Li, T. Zhang, Y. Qin, T. Day, G. Jeffrey Snyder, X. Shi and L. Chen, *J. Appl. Phys.*, 2014, **116**, 203705(1)–203705(8).

40 D. Zhang, J. Yang, Q. Jiang, Z. Zhou, X. Li, J. Xin, A. Basit, Y. Ren and X. He, *Nano Energy*, 2017, **36**, 156–165.

41 F. Liu, J. Zheng, M. Huang, L. He, W. Ao, F. Pan and J. Li, *Sci. Rep.*, 2014, **4**, 1–7.

42 Y. Zhou, Q. Chen, L. Dong and Y. Yin, *Nanosci. Nanotech. Lett.*, 2017, **9**, 1520–1524.

43 R. Chetty, A. Bali and R. C. Mallik, *Intermetallics*, 2016, **72**, 17–24.

44 M.-L. Liu, I.-W. Chen, F.-Q. Huang and L.-D. Chen, *Adv. Mater.*, 2009, **21**, 3808–3812.

45 X. Shi, F. Huang, M. Liu and L. Chen, *Appl. Phys. Lett.*, 2009, **94**, 122103(1)–122103(3).

46 Y. Dong, H. Wang and G. S. Nolas, *Phys. Status Solidi RRL*, 2014, **8**, 61–64.

47 S. Ohno, K. Imasato, S. Anand, H. Tamaki, S. D. Kang, P. Gorai, H. K. Sato, E. S. Toberer, T. Kanno and G. J. Snyder, *Joule*, 2018, **2**, 141–154.

48 S. Ohno, U. Aydemir, M. Amsler, J.-H. Pöhls, S. Chanakian, A. Zevalkink, M. A. White, S. K. Bux, C. Wolverton and G. J. Snyder, *Adv. Funct. Mater.*, 2017, **27**, 1606361(1)–1606361(1).

49 C. Crawford, B. R. Ortiz, P. Gorai, V. Stevanovic and T. S. Eric, *J. Mat. Chem. A - in review*, 2018, **1**, 1–2.

50 E. S. Toberer, P. Rauwel, S. Gariel, J. Taftø and G. J. Snyder, *J. Mat. Chem.*, 2010, **20**, 9877–9885.

51 Y. Tang, Y. Qiu, L. Xi, X. Shi, W. Zhang, L. Chen, S.-M. Tseng, S.-w. Chen and G. J. Snyder, *Energy Environ. Sci.*, 2014, **7**, 812–819.

52 J. Fleurial, L. Gailliard, R. Triboulet, H. Scherrer and S. Scherrer, *J. Phys. Chem. Solids*, 1988, **49**, 1237–1247.

53 D. Kato, K. Iwasaki, M. Yoshino, T. Yamada and T. Nagasaki, *J. Solid State Chem*, 2018, **258**, 93–98.

54 A. Coelho, *Acta Crystallogr., Sect. A: Found. Crystallogr.*, 2007, **63**, 400–406.

55 G. Oszlányi and A. Sütő, *Acta Crystallogr., Sect. A: Found. Crystallogr.*, 2004, **60**, 134–141.

56 G. Oszlányi and A. Sütő, *Acta Crystallogr., Sect. A: Found. Crystallogr.*, 2005, **61**, 147–152.

57 G. Oszlányi, A. Sütő, M. Czugler and L. Párkányi, *J. Am. Chem. Soc.*, 2006, **128**, 8392–8393.

58 W. Kohn and L. J. Sham, *Phys. Rev.*, 1965, **140**, A1133–A1138.

59 G. Kresse and J. Furthmüller, *Phys. Rev. B*, 1996, **54**, 11169–11186.

60 G. Kresse and J. Furthmüller, *Comput. Mater. Sci.*, 1996, **6**, 15–50.

61 P. E. Blöchl, *Phys. Rev. B*, 1994, **50**, 17953–17979.

62 H. J. Monkhorst and J. D. Pack, *Phys. Rev. B*, 1976, **13**, 5188–5192.

63 A. V. Krukau, O. A. Vydrov, A. F. Izmaylov and G. E. Scuseria, *J. Chem. Phys.*, 2006, **125**, 224106(1)–224106(5).

64 J. Heyd, G. E. Scuseria and M. Ernzerhof, *J. Chem. Phys.*, 2003, **118**, 8207–8215.

65 C. Guminski, *J. Phase Equilib.*, 1999, **20**, 344–346.

66 D. Chakrabarti and D. Laughlin, *Bull. Alloy Phase Diagr.*, 1985, **6**, 522–527.

67 H. Okamoto, *J. Phase Equilib.*, 2000, **21**, 496–496.

68 L. Balde, B. Legendre and A. Balkhi, *J. Alloys Compd.*, 1995, **216**, 285–293.

69 Y. Jianrong, N. Silk, A. Watson, A. Bryant and B. Argent, *Calphad*, 1995, **19**, 399–414.

70 R. Sharma, Y. Chang and C. Guminski, *J. Phase Equilib.*, 1995, **16**, 338–347.

71 W. Hume-Rothery, H. Packer, G. Raynor and P. Reynolds, *J. Inst. Met.*, 1940, **66**, 209–239.

72 R. Olesinski and G. Abbaschian, *Bull. Alloy Phase Diagr.*, 1986, **7**, 28–35.

73 A. Pashinkin and V. Fedorov, *Inorg. Mater.*, 2003, **39**, 539–554.

74 R. Blachnik, M. Lasocka and U. Walbrecht, *J. Solid State Chem.*, 1983, **48**, 431–438.

75 T. Koneshova, A. Babitsyna and T. Emel'yanova, *Zhurnal Neorganicheskoj Khimii*, 2001, **46**, 1906–1910.

76 M. Dogguy, C. Carcaly, J. Rivet and J. Flahaut, *J. Less-Common Met.*, 1977, **51**, 181–199.

77 O. Parasyuk, *Pol. J. Chem.*, 1998, **72**, 2440–2449.

78 R. Bacewicz, P. Lottici and C. Razzetti, *J. Phys. C*, 1979, **12**, 3603–3614.

79 L. Gastaldi, M. Simeone and S. Viticoli, *Solid State Commun.*, 1985, **55**, 605–607.

80 G. Antonioli, P. Lottici and C. Razzetti, *Phys. Status Solidi B*, 1989, **152**, 39–49.

81 J. Jaffe and A. Zunger, *Phys. Rev. B*, 1984, **29**, 1882–1906.

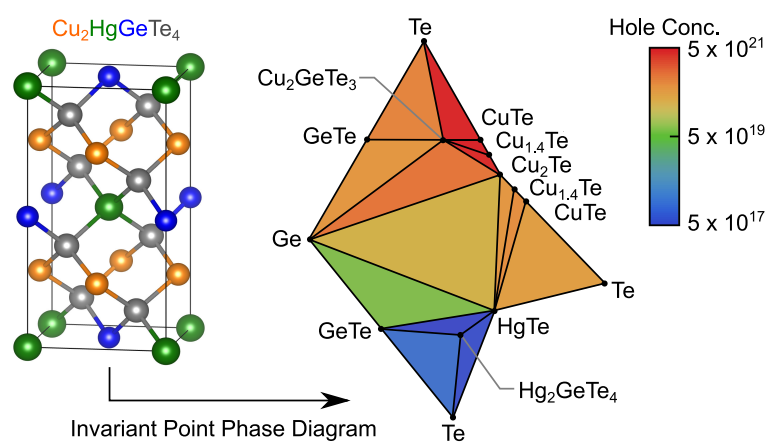82 N. Kim, P. P. Martin, A. A. Rockett and E. Ertekin, *Phys. Rev. B*, 2016, **93**, 165202(1)–165202(9).

Figure 1 Phase boundary mapping in $Cu_2HgGeTe_4$ allows discovery of Hg_2GeTe_4 and further enables carrier density control over 4 orders of magnitude.